

# The climatology of carbon monoxide on Mars as observed by NOMAD nadir-geometry observations

Michael D. Smith<sup>a,\*</sup>, Frank Daerden<sup>b</sup>, Lori Neary<sup>b</sup>, Alain S.J. Khayat<sup>c,a</sup>, James A. Holmes<sup>d</sup>, Manish R. Patel<sup>d,h</sup>, Geronimo Villanueva<sup>a</sup>, Giuliano Liuzzi<sup>f,a</sup>, Ian R. Thomas<sup>b</sup>, Bojan Ristic<sup>b</sup>, Giancarlo Bellucci<sup>g</sup>, Jose Juan Lopez-Moreno<sup>h</sup>, Ann Carine Vandaele<sup>b</sup>

<sup>a</sup> NASA Goddard Space Flight Center, Greenbelt, MD, United States.

<sup>b</sup> Royal Belgian Institute for Space Aeronomy, Brussels, Belgium.

<sup>c</sup> University of Maryland, College Park, MD, United States.

<sup>d</sup> School of Physical Sciences, The Open University, Milton Keynes, United Kingdom.

<sup>e</sup> Space Science and Technology Department, Science and Technology Facilities Council, Rutherford Appleton Laboratory, Oxfordshire, United Kingdom.

<sup>f</sup> American University, Washington, DC, United States.

<sup>g</sup> Istituto di Astrofisica e Planetologia Spaziali, INAF, Rome, Italy.

<sup>h</sup> Instituto de Astrofisica de Andalucia, CSIC, Granada, Spain.

\* To whom correspondence should be addressed:

Michael Smith

Code 693

NASA Goddard Space Flight Center

Greenbelt, MD 20771

(301) 286-7495

[Michael.D.Smith@nasa.gov](mailto:Michael.D.Smith@nasa.gov)

## 1 **Abstract**

2 More than a full Martian year of observations have now been made by the Nadir  
3 Occultation for Mars Discovery (NOMAD) instrument suite on-board the ExoMars  
4 Trace Gas Orbiter. Radiative transfer modeling of NOMAD observations taken in the  
5 nadir geometry enable the seasonal and global-scale variations of carbon monoxide gas in  
6 the Martian atmosphere to be characterized. These retrievals show the column-averaged  
7 volume mixing ratio of carbon monoxide to be about 800 ppmv, with significant  
8 variations at high latitudes caused by the condensation and sublimation of the background  
9 CO<sub>2</sub> gas. Near summer solstice in each hemisphere, the CO volume mixing ratio falls to  
10 400 ppmv in the south and 600 ppmv in the north. At low latitudes, carbon monoxide  
11 volume mixing ratio inversely follows the annual cycle of surface pressure. Comparison  
12 of our retrieved CO volume mixing ratio against that computed by the GEM-Mars  
13 general circulation model reveals a good match in their respective seasonal and spatial  
14 trends, and can provide insight into the physical processes that control the distribution of  
15 CO gas in the current Martian atmosphere.

## 16 **1. Introduction**

17 Carbon monoxide is a minor constituent in the Martian atmosphere, but it plays an  
18 important role in the photochemical cycle of CO<sub>2</sub> production and loss, and it serves as an  
19 important tracer for atmospheric circulation patterns (see Lefèvre and Krasnopolsky,  
20 2017 and references therein for a review). As a non-condensable gas, the volume mixing  
21 ratio (vmr) of CO is expected to have seasonal and spatial variations on a global and  
22 seasonal scale (e.g., Forget et al., 2008; Daerden et al., 2019). Therefore, the seasonal and  
23 spatial variation of CO vmr provides a key observational constraint for understanding the  
24 dynamical and photochemical processes that operate in the current Martian atmosphere.

25 Since its initial detection by Kaplan et al. (1969) using high spectral resolution infrared  
26 spectroscopy, carbon monoxide has been observed in the Martian atmosphere by a  
27 number of ground-based observers at infrared, millimeter, and sub-millimeter  
28 wavelengths (e.g., Clancy et al., 1983; 1990; Lellouch et al., 1991; Krasnopolsky, 2003;  
29 2007; Moreno et al., 2009). These observations had limited seasonal and latitudinal  
30 coverage, but were able to establish an average CO vmr near 800 ppmv and to identify  
31 some latitudinal gradients.

32 Spacecraft observations have provided more information in greater detail about the  
33 seasonal and spatial distribution of CO vmr. Retrievals using observations from the  
34 OMEGA (Encrenaz et al., 2006) and PFS (Billebaud et al., 2009; Sindoni et al., 2011)  
35 instruments on-board the Mars Express spacecraft explored the variation of CO vmr for  
36 certain locations and seasons, while a more complete climatology of CO vmr was  
37 characterized using near-infrared observations made by the CRISM instrument on-board

38 the Mars Reconnaissance Orbiter (Smith et al., 2009; 2018) and using new retrievals  
39 from the PFS observations (Bouche et al., 2021). These works confirmed a global  
40 average CO vmr of about 800 ppmv and revealed the seasonal and spatial patterns  
41 expected for a non-condensable gas, including relatively low CO vmr at the summertime  
42 poles and an anticorrelation with the annual cycle of surface pressure at low latitudes.  
43 Spacecraft observations of CO have been combined with general circulation models  
44 through data assimilation to demonstrate the capability of models in forecasting the  
45 atmospheric state (Holmes et al., 2019).

46 New near-infrared spectra taken in the nadir geometry by the Nadir Occultation for Mars  
47 Discovery (NOMAD) instrument suite (Vandaele et al., 2015; 2018) on-board the  
48 ExoMars Trace Gas Orbiter contain the clear spectral signature of multiple CO  
49 absorption lines and enable the further characterization and refinement of the CO  
50 climatology observed by previous missions. In this paper we present a new climatology  
51 of CO vmr based on radiative transfer modeling of the NOMAD nadir-geometry  
52 observations of CO. These retrievals provide an independent dataset for comparison  
53 against the results found by CRISM and PFS, as well as new information about possible  
54 diurnal variations. We also compare our retrievals of CO vmr against the results  
55 computed using the GEM-Mars general circulation model (Daerden et al., 2015; Neary  
56 and Daerden, 2018; Daerden et al., 2019) to put our results into context and to identify  
57 the physical processes responsible for the observed trends in the CO climatology.

58 In Section 2, we describe the NOMAD instrument and the observations used in this  
59 study. In Section 3 we provide details about the retrieval algorithm including the  
60 assumptions used and the expected uncertainties in the retrieved quantities. The retrieval  
61 results are discussed in Section 4, and in Section 5 we compare the retrieved values  
62 against the output from the GEM-Mars general circulation model. Finally, we summarize  
63 our findings in Section 6.

## 64 **2. Data Set**

### 65 **2.1. NOMAD Instrument**

66 The NOMAD instrument suite was selected for the ExoMars Trace Gas Orbiter mission  
67 in order to provide a spectroscopic survey of the Martian atmosphere that would advance  
68 our knowledge of the composition of the Mars atmosphere (Vandaele et al., 2015; 2018).  
69 The first results from the analysis of NOMAD observations have already been used to  
70 (among other things) set new stringent upper limits on methane abundance (Korablev et  
71 al., 2019) and to evaluate the impact of Mars global dust storms on the D/H ratio  
72 (Vandaele et al., 2019) and the vertical distribution of water vapor (Aoki et al., 2019).

73 NOMAD consists of three different spectrometers that cover large portions of the  
74 ultraviolet, visible, and near-infrared spectral ranges from 0.2 to 4.3  $\mu\text{m}$ . The UVIS

75 (Ultraviolet and Visible Spectrometer) covers the spectral range from 200 to 650 nm  
76 (Patel et al., 2017), while the SO (Solar Occultation) spectrometer is dedicated to solar  
77 occultation observations at near-infrared wavelengths (2.3–4.3  $\mu\text{m}$ ). In this study, we use  
78 the spectra taken by the LNO (Limb Nadir and solar Occultation) spectrometer, which  
79 can be used in both nadir-viewing and limb-viewing geometries, as well as for solar  
80 occultations.

81 The LNO spectrometer is a modified version of the SOIR (Solar Occultation in the IR)  
82 instrument (Nevejans et al., 2006) that was flown on Venus Express (Titov et al., 2006).  
83 It uses an echelle grating in combination with an Acousto-Optical Tunable Filter (AOTF)  
84 to sample the spectral range from 2.3–3.8  $\mu\text{m}$  at a spectral resolving power of roughly  
85 10,000 ( $\sim 0.4 \text{ cm}^{-1}$ ). For each LNO observation, 320 spectral channels cover a spectral  
86 range between 20 and 35  $\text{cm}^{-1}$  depending on the diffraction order. Each order is  
87 characterized by a specific central wavelength, which is selected by the AOTF. A couple  
88 dozen different grating orders are used regularly to monitor different atmospheric  
89 constituents, including carbon monoxide.

## 90 **2.2. Observations Used for this Study**

91 For this work we use all NOMAD LNO observations taken using grating orders 189 and  
92 190 (4250–4300  $\text{cm}^{-1}$ , or 2325–2350 nm), which are used specifically to monitor carbon  
93 monoxide. Although solar occultation observations have greater sensitivity and enable  
94 the vertical distribution to be retrieved, the nadir-geometry observations used here have  
95 the advantage of higher horizontal spatial resolution and much more complete seasonal  
96 and (horizontal) spatial coverage. Where available, the LNO observations consist of  
97 north-south strips across the entire visible disk of Mars containing up to a couple hundred  
98 individual spectra for each orbit. The projected instantaneous LNO footprint on the  
99 surface of Mars is approximately 0.5 x 17 km (Vandaele et al., 2015), and observations  
100 are typically spaced every  $\sim 0.7^\circ$  of latitude along the orbit track. At the near-IR  
101 wavelengths used here we depend on reflected solar light for our signal and the  
102 contribution from thermal radiation is negligible. Therefore, we cannot retrieve carbon  
103 monoxide for nighttime or winter polar regions, and in addition, observations with solar  
104 incidence angle greater than  $55^\circ$  are not used because of their low signal-to-noise.

105 The NOMAD LNO observations used in this study cover the time period between Mars  
106 Year (MY) 34,  $L_s=150^\circ$  and MY 35,  $L_s=241^\circ$  (28 March 2018 and 18 July 2020). This  
107 time period covers more than a complete Mars Year, with overlapping coverage between  
108 two Mars Years during the peak dustiest season when some observations were not used  
109 because of excessive atmospheric dust loading (see Section 3.4).

110 Figure 1 shows the coverage of the 109,159 retrievals used in this work as a function of  
111 season ( $L_s$ ) and latitude. During each period of time when nadir observations are possible

112 (each lobe in Figure 1) the local time of the observations changes systematically from late  
113 afternoon to early morning. The solar incidence angle is lowest in the center and  
114 increases outward to the edge of each lobe. Observations were taken sufficiently often to  
115 enable a good characterization of the seasonal and global-scale trends in carbon  
116 monoxide volume mixing ratio, but are not capable of providing maps on short timescales  
117 on the order of days or weeks. Observations using both NOMAD grating orders 189 and  
118 190 were taken throughout the time period shown in Fig. 1.

119 A typical set of spectra taken using order 190 on one orbit is shown in Fig. 2. In this  
120 image each spectrum is represented by a horizontal row in the image with color  
121 indicating the observed signal. The quantity that is shown here and that is used in this  
122 analysis is the “Reflectance Factor” field provided by the nominal NOMAD data pipeline  
123 processing (further detail about the calibration of NOMAD data can be found in Liuzzi et  
124 al., 2019; Thomas et al., 2020). This divides the observed radiance of Mars by the  
125 observed solar reference spectrum with corrections for the Mars-Sun distance and mean  
126 solar incidence angle. The wavelength of each NOMAD channel depends on the  
127 instrument temperature at the time of each measurement (e.g., Liuzzi et al., 2019), so a  
128 wavelength correction is performed for each individual observation as a part of the  
129 retrieval by fitting the observed lines to their known wavelengths. The individual  
130 absorption lines caused by CO are readily apparent as vertical bands in Fig. 2 (for  
131 example, at 4285.0, 4288.3, and 4291.5  $\text{cm}^{-1}$ ).

### 132 **3. Retrieval Algorithm**

133 We use seven lines for the retrieval of carbon monoxide using NOMAD LNO  
134 observations from the (2-0) ro-vibrational band, with four lines from order 189 (R0, R1,  
135 R2, and R3) and three from order 190 (R6, R7, and R8). As shown in Fig. 3., the CO  
136 absorption lines in this spectral region are very well separated from each other and from  
137 any other significant absorptions from water vapor or CO<sub>2</sub>. At the spectral resolution of  
138 the LNO observations, the absorptions have a depth that is typically at a level of 5–10%  
139 of the continuum level, which is more than sufficient for a reliable retrieval. These CO  
140 lines are part of the same absorption band used for retrievals of CO by the CRISM  
141 instrument (Smith et al., 2009; 2018).

#### 142 **3.1. Radiative Transfer and Assumptions**

143 The radiative transfer modeling used here for computing synthetic spectra of carbon  
144 monoxide is essentially the same as that used in our previous retrievals using CRISM  
145 spectra (Smith et al. 2009; 2018). To perform the retrieval, radiative transfer modeling is  
146 used to compute an expected spectrum for a given volume mixing ratio of carbon  
147 monoxide, and that CO vmr is then varied until the resulting integrated line depth of the

148 CO absorptions in the computed spectrum matches that from the observed NOMAD LNO  
149 spectrum.

150 The radiative transfer is modeled using the discrete ordinates approach (e.g., Goody,  
151 1989; Thomas and Stamnes, 1999), which explicitly includes multiple scattering by  
152 aerosols. Absorption of carbon monoxide gas is computed using the correlated-k  
153 approximation (Lacis and Oinas, 1991), using the latest version of the HITRAN  
154 spectroscopic database for line parameters, which now include line broadening from  
155 carbon dioxide (Gordon et al., 2017). The viewing geometry, including the solar  
156 incidence angle, the emergence angle, and phase angle are read from spacecraft records  
157 and are assumed to be known quantities.

158 The thermal state of the atmosphere for each observation is provided by the OpenMARS  
159 database, which is a reanalysis product that combines spacecraft observations with a  
160 Mars General Circulation Model (Holmes et al., 2020). Thus, the temperature profiles  
161 read from OpenMARS and used in this work include the effects of the global dust storm  
162 that occurred during Mars Year 34 (e.g., Guzewich et al., 2018; Smith, 2019). Surface  
163 pressure is taken from the Mars Climate Database v.5.3 (Forget et al., 1999; Millour et  
164 al., 2018) using its high-resolution setting to resolve sub-grid topography. Surface albedo  
165 is taken from a map based on Thermal Emission Spectrometer observations (Christensen  
166 et al., 2001).

167 Scattering from dust and water ice aerosols affects the observed depth of gas absorptions  
168 and must be included in the model for an accurate retrieval. The optical depth of dust and  
169 water ice aerosols for each NOMAD LNO spectrum is estimated from concurrent  
170 observations by the THEMIS instrument on Mars Odyssey (Smith, 2018; 2019). The  
171 scattering properties of dust and water ice aerosols are taken from the analysis of CRISM  
172 near-infrared observations (Wolff et al., 2009), while the aerosol particle size (effective  
173 radius of 1.5  $\mu\text{m}$  for dust and 2.0  $\mu\text{m}$  for water ice) is an average value from the analysis  
174 of many previous spacecraft observations (e.g., Wolff and Clancy, 2003; Clancy et al.,  
175 2003; Wolff et al. 2006; 2009; Vincente-Retortillo, 2017). The dust aerosol is assumed  
176 here to be well-mixed with the background atmosphere. Water ice aerosol is assumed to  
177 form clouds above the water condensation level, with no cloud below and a well-mixed  
178 cloud above. Discussion of the uncertainties related to the above assumptions is presented  
179 in Section 3.4.

### 180 **3.2. Retrieval Algorithm Process**

181 Figure 4 shows representative averaged NOMAD LNO spectra for the seven lines chosen  
182 for the retrieval. The center locations for these lines for order 189 are: 4263.8, 4267.5,  
183 4271.2, and 4274.7  $\text{cm}^{-1}$ , and for order 190 are: 4285.0, 4288.3, and 4291.5  $\text{cm}^{-1}$ . For  
184 each line, we divide the observed reflectance factor by the continuum level and compute

185 the total integrated line depth for the line. The integrated line depth retains all the  
186 information from the line since these lines are spectrally unresolved in the observations.  
187 The observation to be fit is then the sum of the integrated line depths for all of the lines in  
188 each spectrum.

189 The retrieved value of CO volume mixing ratio is determined by computing synthetic  
190 spectra with a given CO vmr and computing the integrated line depth for the three or four  
191 lines in the computed spectrum (with the continuum divided out) in the same way as done  
192 for the observation. In the computation, CO is assumed to be well-mixed vertically,  
193 which is supported by previous studies (e.g., Smith et al., 2019) and by model results for  
194 the lower part of the atmosphere where most of the CO molecules lie (e.g., Daerden et al.,  
195 2019). The final retrieved value of CO vmr is simply that value where the computed  
196 integrated line depth matches the observed value.

197 Using this algorithm makes the retrieval robust to uncertainties in the instrumental  
198 spectral response function and to errors or uncertainties in the overall calibration of the  
199 observed reflectance factor. The drawback of using integrated line depth as a metric is its  
200 sensitivity to the choice of the continuum. To minimize this sensitivity, we define the  
201 continuum as being linear in reflectance factor and computed using spectral channels that  
202 are the same constant distance (plus and minus 6 LNO channels, or about  $\pm 0.64 \text{ cm}^{-1}$ )  
203 from the line center for each line. These computed continua are shown in Fig. 4 as red  
204 line segments.

205 Along with the retrieved value of CO vmr, for each spectrum we also record the observed  
206 noise level in the observation by computing the root mean square (rms) variation of the  
207 reflectance factor in the spectral regions between the lines used in the retrieval. This  
208 quantity is used as a quality control parameter. Retrievals with a noise level greater than a  
209 threshold value are rejected.

### 210 **3.3. Modeling the AOTF**

211 The presence of the AOTF complicates modeling of the observed NOMAD spectrum  
212 since the observed signal for a given diffraction order will also contain some amount of  
213 signal from neighboring orders. Since the CO absorption lines used for this analysis are  
214 well spaced with essentially no contribution from other species (Fig. 3), the main concern  
215 is the addition of continuum signal from neighboring orders to the observed signal of the  
216 CO lines in the orders being studied. The effect of adding this continuum from  
217 neighboring orders would be to artificially reduce the integrated line depth that we use as  
218 our observation to be retrieved, and thus to systematically reduce the CO vmr values that  
219 we retrieve.

220 Fortunately, this effect is observed to be relatively small for the NOMAD LNO  
221 observations in orders 189 and 190 that are used for our CO retrievals. Ideally,

222 absorptions that are very optically thick at the spectral resolution of NOMAD would be  
223 used to estimate this out-of-order continuum contribution. In this case, the expected  
224 signal would be zero inside the absorption and any non-zero signal that is observed could  
225 be attributed to the continuum from other orders. There are no such optically thick  
226 absorptions for these diffraction orders, so instead we use two different means to estimate  
227 the contribution from neighboring orders.

228 The most straightforward method is to look at the relative amplitude of spectral lines  
229 aliased from neighboring orders by the AOTF. Figure 5 shows four of the same spectra  
230 for order 189 as shown in Fig. 4. The black vertical lines indicate the frequency of the  
231 CO absorptions for order 189. As expected, they line up with the observed spectral  
232 features. The red and blue vertical lines indicate the frequencies where we would expect  
233 to see CO absorptions aliased from orders 188 (red lines) and 190 (blue lines) by the  
234 AOTF. Spectral features aliased from neighboring orders are clearly visible in many  
235 NOMAD observations, for example, the solar occultation observations analyzed by Aoki  
236 et al., (2019), and the analysis of Liuzzi et al., (2019). However, the LNO observations  
237 for orders 189 and 190 show essentially no features at the expected locations, which  
238 indicates that the contribution from other orders is small.

239 The top panel of Fig. 6 shows how comparing the observed line depth of a CO absorption  
240 aliased from a neighboring order ( $4268.8 \text{ cm}^{-1}$ , the middle blue line in Fig. 5) against the  
241 observed line depth of a CO absorption from the order being observed ( $4267.55 \text{ cm}^{-1}$ , the  
242 middle black line in Fig. 5) can be used to estimate the continuum contribution from  
243 neighboring orders. The greater the observed line depth ratio, the greater the contribution  
244 from neighboring orders, and the smaller the line depth would be for the CO lines used in  
245 the retrieval. A detailed analysis looking at all the LNO order 189 observations shows  
246 this observed line depth ratio to be no larger than 0.02. Using Fig. 6, this implies that the  
247 observed CO lines used in this retrieval are at least 0.92 times as strong as they would be  
248 with no AOTF. In other words, the true CO line depths at Mars (with no AOTF) are at  
249 most 1.08 times stronger than observed.

250 A second way to estimate the out-of-order continuum contribution is to look at how  
251 retrieved CO varies as a function of a known quantity where the expected variation is  
252 non-linear. The variation of CO with surface pressure is the best example of this. Surface  
253 pressure is (essentially) known from model results, and the expected line depth of CO  
254 varies non-linearly with surface pressure both because the curve of growth is non-linear  
255 (i.e., doubling the amount of CO leads to a line depth less than twice as large) and  
256 because of the effects of pressure broadening of the absorption lines.

257 The bottom panel of Fig. 6 shows the results of a numerical experiment where we use a  
258 constant CO vmr and a range of surface pressures to compute expected line depths. We  
259 multiply each of these line depths by factors ranging from 0.9 to 1.0 (as indicated in Fig.



260 6 by the numbers at the ends of the black curves) and then perform the retrieval on these  
261 reduced “observed” line depths assuming no AOTF. The results, normalized to their  
262 value at 6 mbar, show a systematic variation with surface pressure. The actual CO  
263 retrievals using NOMAD LNO observations (presented in detail in Section 4) for orders  
264 189 and 190 are shown by the red and blue points. Here we have used only retrievals  
265 between 30° S and 30° N latitude to minimize real variations of CO vmr, and we have  
266 smoothed the results by convolving with a function 1 mbar wide in surface pressure. As  
267 expected, the retrievals do show a tendency toward lower CO vmr values at lower surface  
268 pressures, but the implied continuum contribution from other orders is not large, with the  
269 resulting strength of the observed CO lines being at least 0.95 times as strong as they  
270 would be with no AOTF.

271 Taken together, the two independent analyses above present strong evidence that the  
272 AOTF contribution to the continuum from neighboring orders is relatively minor for the  
273 specific case of the LNO observations for orders 189 and 190. Again, we note that AOTF  
274 is observed to produce significant contributions from neighboring orders for other orders  
275 and modes (e.g., Liuzzi et al., 2019; Aoki et al., 2019). For this case of these retrievals,  
276 the observations are consistent with the CO lines being at least 0.92-0.95 times as strong  
277 as they would be with no AOTF. Therefore, for simplicity we have chosen to not include  
278 the AOTF in our retrieval. Systematically underestimating line depths by 5–8% would  
279 lead to a systematic underestimate of retrieved CO by as much as 20%. However, any  
280 such effect of the AOTF not accounted for in the retrieval would be a nearly constant  
281 factor applied to every individual retrieval, so that while this uncertainty would affect the  
282 overall average CO vmr it would have essentially no effect on the seasonal and latitudinal  
283 variations of CO that are the focus of this work.

#### 284 **3.4. Uncertainties**

285 In addition to uncertainties from the AOTF, there are a number of other sources that  
286 could contribute systematic uncertainties. Given the form of our retrieval algorithm, the  
287 uncertainty in retrieved results is most easily estimated through the use of numerical  
288 experiments. For each source of uncertainty to be evaluated, the retrieval algorithm can  
289 be performed over a range of different assumptions, approximations, or values to evaluate  
290 the resulting change in the retrieved volume mixing ratio of carbon monoxide.

291 The most straightforward quantities to test are model-related assumptions, such as the  
292 number of vertical layers in the model, the number of radiation streams included in the  
293 discrete ordinates formulation, and the number of terms kept in the Legendre polynomial  
294 expansion of the scattering phase functions. These parameters can be set large enough so  
295 that they do not contribute significantly to the total uncertainty. In each case the model  
296 parameters were chosen so that the retrieved CO vmr changed by less than one percent  
297 when the number of model layers, radiation streams, or phase function terms was

298 doubled. The actual values used in the retrieval are 16 radiation streams, 32 terms in the  
299 Legendre polynomial expansion, and 25 vertical layers in the model.

300 Although thermal radiation is negligible in these observations, atmospheric temperatures  
301 can still affect the retrievals since the spectroscopic properties of CO, including line  
302 strengths and widths, are temperature dependent. Since we use atmospheric temperatures  
303 from OpenMARS that are specifically computed from assimilation of observations during  
304 Mars Years 34 and 35, we expect them to be well within 10 K of the true value for all  
305 cases. As a test of the worst case, we found that an offset in the temperature profile by 10  
306 K over the entire atmosphere leads to a 2–6% change in retrieved CO vmr.

307 It is not possible to reliably retrieve aerosol optical depth from the individual NOMAD  
308 LNO spectra themselves because of the very limited spectral range in each spectral order.  
309 However, the use of dust and water ice aerosol optical depth from concurrent THEMIS  
310 observations provides a useful estimate. Numerical experiments show that doubling the  
311 aerosol optical depth found outside of major dust storms leads to changes in the retrieved  
312 CO vmr by 5% or less. During large dust storms the optical depth of the dust can become  
313 large enough to effectively screen the lower part of the atmosphere so that the entire  
314 column is not sampled by the observations. For this reason, we choose to reject any  
315 observation for which the extinction optical depth at 9- $\mu\text{m}$  is greater than unity. This  
316 corresponds to an extinction optical depth at the wavelength used in this retrieval of about  
317 1.8. Our assumptions for the vertical profile of dust and water ice aerosol are found by  
318 numerical experiment to cause changes in the retrieved values by 10% or less for any  
319 reasonable choices.

320 Uncertainty related to our definition of the continuum level was tested by performing the  
321 retrieval for a large suite of cases using different offsets from the line center for  
322 computing the continuum (including cases with asymmetric offsets). The retrieval results  
323 were found to vary by as much as 10% for reasonable choices for the definition of the  
324 continuum. Considering all of the above sources of uncertainty, we estimate that the total  
325 systematic one-sigma uncertainty in an individual retrieval of CO vmr to be 20% or less  
326 from sources other than the AOTF.

327 Perhaps the most straightforward way to estimate an overall uncertainty estimate is by  
328 looking at the retrieval values themselves. In addition to the uncertainties described  
329 above, the amplitude of random noise in the observed spectra relative to the observed  
330 continuum level varies significantly as a function of solar incidence angle, surface  
331 albedo, and the distance between Mars and the Sun. As mentioned earlier, we compute  
332 the amplitude of the random noise relative to the continuum level for each spectrum to  
333 use as a quality criterion. We select the maximum allowed value for the noise level based  
334 on a tradeoff between the desire to retain as many retrievals as possible, while keeping  
335 the observation-to-observation variation of retrieved CO vmr to a minimum.

336 For a given maximum allowed value for the noise level, we compute the rms difference  
337 between individual retrievals and a smoothed average formed by a 2-D convolution of the  
338 retained retrievals using a bin size  $45^\circ$  in  $L_s$  and  $15^\circ$  in latitude. Figure 7 shows the results  
339 for this analysis, which was performed separately for retrieval results from orders 189  
340 and 190. For the strictest cases (lowest maximum allowed noise level) the fraction of the  
341 retrievals retained is low, but the overall uncertainty in the retrievals estimated by the rms  
342 from their smoothed average is also relatively low. As the noise level criterion is relaxed  
343 to allow retrievals from observations with higher noise levels, progressively more  
344 retrievals are retained at the cost of more scatter in the retrieval results. Given the  
345 relatively gradual slopes in Fig. 7, we select values (indicated by arrows) for the  
346 maximum allowed noise level to retain 85-90% of the retrievals. Specifically, we set the  
347 maximum allowed noise level relative to the continuum level to be 0.025 for order 189  
348 and 0.035 for order 190. This leads to our best estimate for the overall uncertainty in  
349 individual retrievals of CO vmr to be about 240 ppmv for order 189 and 290 ppmv for  
350 order 190. Given that the global, seasonal average is about 800 ppmv (see section 4), this  
351 corresponds to 30–35%, which is comparable to or slightly better than that for the  
352 CRISM retrievals of CO vmr (Smith et al., 2009; 2018). This total uncertainty is larger  
353 enough than the 20% systematic uncertainty described above that these retrievals are not  
354 dominated by systematics.

## 355 **4. Retrieval Results**

356 Here we present the results of the retrieval of the column-integrated carbon monoxide  
357 volume mixing ratio for all NOMAD LNO observations using orders 189 and 190 taken  
358 between Mars Year (MY) 34,  $L_s=150^\circ$  and MY 35,  $L_s=241^\circ$  (28 March 2018 and 18 July  
359 2020). This covers 1.25 Mars Years, providing a climatological view of CO and its  
360 seasonal and spatial variations. Excluded are observations with a solar incidence angle  
361 greater than  $55^\circ$ , those taken during major dust storms, and those with noise levels that  
362 exceed the threshold value given in the previous section. These retrieval results are  
363 available for download at <http://dx.doi.org/10.17632/px89dk6ck9.1>

### 364 **4.1. Climatology of Retrieved Carbon Monoxide**

365 The retrieved column-integrated carbon monoxide volume mixing ratio is shown in Fig. 8  
366 as a function of season ( $L_s$ ) and latitude separately for the retrievals using order 189 and  
367 190. As described above in detail, the uncertainty in individual retrieved values are  
368 relatively large (30–35%) so the CO vmr shown in Fig. 8 has been smoothed to highlight  
369 the trends. The size of the smoothing box is  $15^\circ$  in  $L_s$  and  $15^\circ$  in latitude and is shown in  
370 the figure for comparison. In total, there are 34,152 retrievals for order 189 and 75,007  
371 retrievals for order 190.

372 The overall level of CO vmr and its seasonal and latitudinal variations are broadly similar  
373 between the two orders. While there are minor differences, perhaps most notably the  
374 generally higher CO vmr in order 189 retrieved around  $L_s=180^\circ$ , these differences are  
375 well within the stated uncertainties and do not appear from our analysis to arise from any  
376 systematic differences between the two orders. Therefore, from this point forward we will  
377 describe the combined results from each of the two orders under the assumption that this  
378 provides the most accurate value possible.

379 The CO climatology displayed in Fig. 8 bears a strong resemblance to those retrieved  
380 previously from CRISM (Smith et al., 2008; 2019) and from Mars Express PFS (Bouche  
381 et al., 2021), and is largely as expected for a non-condensable gas (e.g., Forget et al.,  
382 2008; Daerden et al., 2019; Holmes et al., 2019). There is depletion of carbon monoxide  
383 in the summertime polar regions in both hemispheres, although it is significantly stronger  
384 in the south. The southern hemisphere summertime depletion leads to CO vmr values of  
385 400 ppmv or less poleward of  $70^\circ\text{S}$ , while in the north at least  $\sim 600$  ppmv of CO is  
386 maintained at all observed locations. In both hemispheres the minimum CO vmr values  
387 are found somewhat before solstice (by up to  $\sim 30^\circ$  of  $L_s$ ), especially at latitudes further  
388 removed from the pole. The summertime depletion of CO extends to roughly  $40^\circ$  latitude  
389 in both hemispheres, with a roughly constant gradient at higher latitudes trending to  
390 lower CO vmr toward the pole. Model results indicate a corresponding maximum in CO  
391 vmr over the winter poles (Forget et al., 2008; Daerden et al., 2019; Holmes et al., 2019),  
392 but this cannot be directly confirmed with retrievals using NOMAD LNO, which rely on  
393 solar illumination for the observed signal.

394 The NOMAD LNO retrievals show that the CO vmr at low latitudes follows a seasonal  
395 variation that ranges between roughly 700 ppmv near  $L_s=0^\circ$  and 900–950 ppmv near  
396  $L_s=180^\circ$ , with an annually averaged value near 800 ppmv. Moving from south to north,  
397 the peak annual value tends to occur at gradually later seasonal dates, from about  
398  $L_s=140^\circ$  at  $30^\circ\text{S}$  latitude to about  $L_s=220^\circ$  at  $30^\circ\text{N}$  latitude (this trend is more easily  
399 seen in the combined and smoothed version of the retrievals discussed in Section 5.1 and  
400 shown in Fig. 10). As expected for a non-condensable gas, the overall seasonal variation  
401 of CO vmr is observed to roughly follow an inverse relation with the annual variation of  
402 surface pressure observed from the surface of Mars (e.g., Tillman et al., 1993; Martínez  
403 et al., 2018), although the pattern is also modified by the latitudinal transport of CO (e.g.,  
404 Daerden et al., 2019; Smith et al., 2018) as will be further discussed in Section 5.3.

405 Given the relatively long chemical lifetime of CO lived ( $\sim 6$  years; Krasnopolsky, 2007),  
406 we do not expect to see interannual variations in these retrievals. The differences between  
407 the MY 34 retrievals at the beginning of the time period shown in Fig. 8 and the MY 35  
408 retrievals at the end are instead indicative of the level of uncertainty in the retrievals.

## 409 **4.2. Spatial and Diurnal Variations of Retrieved Carbon Monoxide**

410 Figure 9 shows maps of the spatial variation of CO vmr for the four cardinal seasons of  
411 the Martian year. To attempt to identify trends, a spatial smoothing has been performed  
412 using a box  $45^\circ$  in longitude by  $15^\circ$  in latitude. The largest variations are the latitudinal  
413 gradients that describe the annual climatology described in the previous section. At  
414  $L_s=270^\circ$  there is a clear gradient from higher values of CO vmr in the north where it is  
415 winter to lower values in the south where it is summer.

416 Overall, there appears to be limited variation of CO vmr with longitude. The relative lack  
417 of correlation between CO vmr and surface topography supports our assumption that CO  
418 is largely well-mixed, at least in the lower portion of the atmosphere containing the bulk  
419 of the column mass. Most of the small amplitude longitudinal variations that do appear in  
420 Fig. 9 are not statistically significant and do not correspond to features in similar maps of  
421 CO vmr based on CRISM retrievals presented in Smith et al. (2018). The exception is  
422 that the Hellas region at  $L_s=90^\circ$  stands out as having a higher CO vmr than neighboring  
423 locations. This enhancement in Hellas during winter was also observed in CRISM  
424 retrievals of CO (Smith et al., 2018), although the corresponding enhancements observed  
425 in regions with low-lying topography in the north at  $L_s=270^\circ$  are not observed in the  
426 LNO retrievals shown here.

427 Recalling the top panel of Fig. 1, the precessing orbit of the Trace Gas Orbiter enables  
428 NOMAD to view a range of local times between roughly 08:00 and 16:00 local true solar  
429 time over a relatively short seasonal timescale. However, our analysis of the retrievals  
430 does not reveal any systematic variation of column-integrated CO vmr as a function of  
431 local time at levels greater than 10%, at least for the daytime hours observable by  
432 NOMAD LNO.

## 433 **5. Discussion**

### 434 **5.1. Comparison with CRISM and Other Previous Results**

435 The retrievals of carbon monoxide volume mixing ratio from this work can be directly  
436 compared against previous retrievals from other spacecraft observations. In particular, we  
437 focus here on a comparison against the retrievals from CRISM, which use the same CO  
438 absorptions and have a similar uncertainty level (Smith et al., 2009; 2018). The CRISM  
439 observations were taken from MY 28 to 33. The top two panels in Fig. 10 show a side-  
440 by-side comparison of the CO climatology retrieved from CRISM and the current work.  
441 For ease of comparison, each has been smoothed with a box  $45^\circ$  in  $L_s$  and  $15^\circ$  in latitude  
442 to highlight global/seasonal trends, and the CRISM climatology has been resampled to  
443 the same  $L_s$  and latitude values as given by the NOMAD LNO retrievals.

444 The overall annual average value is roughly the same in the NOMAD LNO and CRISM  
445 retrievals at 800 ppmv. And, the overall pattern of variation described in Section 4.1, with  
446 reduced CO vmr near the south pole during summer solstice, a smaller reduction in CO

447 vmr near the north pole during summer solstice, and low-latitude CO vmr inversely  
448 correlated with the annual cycle of surface pressure, is observed in both the NOMAD  
449 LNO and the CRISM datasets. However, one difference is that the amplitude of the  
450 variations is noticeably less in the NOMAD LNO retrievals, being perhaps half as large  
451 as that in the CRISM retrievals.

452 Other differences are present, but smaller. The northern summer minimum in the CRISM  
453 retrievals is more extensive than in the NOMAD LNO retrievals, both in terms of  
454 latitudinal extent and seasonal duration. On the other hand, the southern summer  
455 minimum has very similar latitudinal extent and seasonal duration in the two datasets.  
456 The NOMAD LNO retrievals tend toward somewhat greater CO vmr values than those  
457 from CRISM at low northern latitudes during the second half of the Martian year  
458 ( $L_s=180^\circ-360^\circ$ ) and do not show the slight decrease apparent in CRISM southern  
459 hemisphere retrievals between  $L_s=0^\circ$  and  $120^\circ$ .

460 Recently, another climatology of CO vmr has been retrieved using observations from the  
461 Planetary Fourier Spectrometer (PFS) on the Mars Express spacecraft (Bouche et al.,  
462 2021) spanning MY 26 to 34. This retrieval uses a different set of CO absorptions at  
463  $\sim 2100\text{ cm}^{-1}$  ( $4.7\ \mu\text{m}$ ), but are still directly comparable to the NOMAD LNO results.  
464 Bouche et al. (2021) find an overall annual average CO vmr of 820 ppmv and many of  
465 the same climatological variations described above. Their southern summer minimum has  
466 a somewhat smaller amplitude ( $\sim 500$  ppmv for PFS,  $\sim 400$  ppmv for NOMAD LNO), but  
467 the northern summer minimum is somewhat deeper ( $\sim 600$  ppmv for PFS,  $\sim 650$  ppmv for  
468 NOMAD LNO) and there is a larger annual variation at low latitudes in the PFS  
469 retrievals.

470 It is unlikely that the observed differences between the CRISM, PFS, and NOMAD  
471 retrievals are caused by real interannual variations in CO vmr. The chemical lifetime for  
472 CO is relatively long, and the different retrievals are generally within the uncertainties of  
473 the different retrievals. Furthermore, all three of the climatologies compared here (from  
474 NOMAD, CRISM, and PFS) are of retrieved values that have been averaged over all  
475 Mars Years observed by each instrument.

## 476 **5.2. Comparison with GCM Modeling Results**

477 The retrievals of CO vmr from the NOMAD LNO observations can also be compared  
478 against model results. Such a comparison can provide insight into the physical processes  
479 that drive the observed climatology, and differences between observations and model  
480 results can identify areas where improvement is needed in the model or retrieval process.

481 The model used here is the GEM-Mars General Circulation Model (Daerden et al., 2015;  
482 Neary and Daerden, 2018; Daerden et al., 2019). This model uses 103 vertical levels  
483 extending from the surface to  $\sim 150$  km, and it is operated on a grid with a horizontal

484 resolution of  $4^\circ \times 4^\circ$  in latitude and longitude. More details on the physical  
485 parameterizations in the model and evaluations of simulations are provided in Neary and  
486 Daerden (2018), Smith et al. (2018), Daerden et al. (2019), Neary et al. (2020), and  
487 Bouche et al. (2021). Here we summarize the parameterization for the non-condensable  
488 gas enrichment. Deposition (sublimation) of  $\text{CO}_2$  above a model point results in a change  
489 of the surface pressure. The dynamical core of the GCM then readjusts the atmospheric  
490 mass globally, and the impact of the mass loss at the poles is spread out instantaneously  
491 over the entire planet. Locally, the enrichment (or depletion) of minor species will build  
492 up more gradually and spread out on a longer timescale by eddy mixing and global  
493 circulation. Because of the definition of the model levels in a GCM in terms of surface  
494 pressure (implying that the model levels themselves will be modified upon deposition or  
495 sublimation), this local process is difficult to disentangle from the global pressure  
496 correction. Forget et al. (2008) and Lian et al. (2012) developed methods to treat this  
497 problem in their GCMs. In GEM-Mars we apply a simple parameterization that corrects  
498 the local vmr after deposition (or sublimation) in two steps. First the vmr of  $\text{CO}_2$  is  
499 modified at all model levels by a single factor that corrects its column abundance to  
500 match the local surface pressure change. Then it is additionally modified at those vertical  
501 model levels where  $\text{CO}_2$  ice deposition occurred, by a factor that is proportional to the  
502 vmr of condensing (or sublimating) ice particles. The factors of proportionality (one for  
503 deposition and one for sublimation, see Smith et al. (2018) and Bouche et al. (2021) for  
504 details) do not necessarily have the same values, as they describe different processes that  
505 involve different timescales, but they should be well balanced to ensure that the total  
506 atmospheric content of noncondensing species does not change.

507 For the simulations presented here, the atmospheric dust was constrained by the dust  
508 climatologies provided by Montabone et al. (2015, 2020). For total CO columns, no  
509 significant difference was found between using the dust climatology for a year with  
510 nominal dust loading (e.g., MY 33) and using the observed dust climatology for MY 34  
511 (when the early NOMAD observations were taken), which included a global dust storm  
512 (e.g., Smith, 2019). It was found that the global dust storm had an impact on the higher  
513 altitude photochemistry through the redistribution of water vapor (Neary et al., 2020),  
514 and therefore also on CO vmr in the upper atmosphere, but did not have an impact on the  
515 lower atmospheric CO and on the total column amounts such as retrieved by NOMAD  
516 LNO observations.

517 The bottom two panels of Fig. 10 show a comparison of CO vmr climatology as retrieved  
518 by NOMAD LNO observations against that computed by GEM-Mars. Here, the overall  
519 average initial value of CO vmr has been adjusted in the model, compared to the results  
520 shown in Smith et al. (2018), to match the NOMAD observations, so it is the seasonal  
521 and latitudinal variations that should be compared. The GEM-Mars model closely  
522 matches the observed climatological patterns. In particular, the southern summer

523 minimum is well represented as is the modest increase in low-latitude CO vmr between  
524  $L_s=120^\circ$  and  $210^\circ$  in response to the annual minimum in surface pressure. The amplitudes  
525 of those two features as computed by GEM-Mars are more similar to those observed by  
526 NOMAD LNO than to the larger amplitude features observed by CRISM. Perhaps the  
527 largest difference between the model and the retrievals is the northern summer minimum.  
528 The NOMAD LNO retrievals show a much smaller decrease than the CRISM retrievals,  
529 but the minimum in the GEM-Mars has even smaller amplitude.

530 Figure 11 shows a comparison between the NOMAD LNO retrievals and the GEM-Mars  
531 model results in some more detail. Both datasets have been binned in latitude bands as  
532 stated, and then binned in  $L_s$  using a box  $15^\circ$  wide sliding  $5^\circ$  of  $L_s$  between each point.  
533 Again, there is a close correspondence with the largest differences being at high northern  
534 latitudes where the model predicts higher CO vmr than observed, and a smaller latitudinal  
535 gradient at low latitudes ( $-40^\circ$  to  $+40^\circ$ ) during the second half of the Martian year  
536 ( $L_s=180^\circ$ – $360^\circ$ ). The remaining differences, with a root-mean-square amplitude of  $\sim 50$   
537 ppmv, are within the noise level in the retrievals.

538 In general, the GEM-Mars General Circulation Model can reproduce the relative  
539 distribution of the observed climatology of CO vmr and explain its broad features  
540 (Daerden et al., 2019). Carbon monoxide is a relatively long-lived ( $\sim 6$  years;  
541 Krasnopolsky, 2007) and non-condensable species. As such, we do not expect significant  
542 interannual variations, and the column-averaged volume mixing ratio of CO is controlled  
543 by the condensation of  $\text{CO}_2$  and latitudinal transport. The condensation of  $\text{CO}_2$  onto the  
544 southern seasonal cap during winter is followed by this CO-enriched air being transported  
545 equatorward and into the northern hemisphere between  $L_s=120^\circ$  and  $180^\circ$  forming the  
546 low-latitude maximum in CO vmr that is observed. Sublimation of the seasonal  $\text{CO}_2$  cap  
547 during Spring and Summer releases large amounts of  $\text{CO}_2$  leading to a minimum in CO  
548 vmr. The amount of  $\text{CO}_2$  condensed onto the southern cap is much greater than that  
549 condensed onto the northern cap, which explains the difference in the amplitude of the  
550 two summertime minima in CO vmr. Assimilation of the CO climatology observed by  
551 NOMAD LNO could help improve the parameterization of model processes and thereby  
552 reduce the difference between the model and retrieval results, which is the subject of  
553 active research.

## 554 **6. Summary**

555 The nadir-geometry LNO observations taken by the NOMAD instrument enable the  
556 characterization of the climatology of the column-averaged volume mixing ratio of  
557 carbon monoxide gas in the Martian atmosphere. Comparison of these retrieved values  
558 with the results from the GEM-Mars GCM model allow for physical interpretation of the  
559 retrieved seasonal and spatial variations, and also serve to highlight possible areas for  
560 improvement in both the model and the retrieval process.



561 NOMAD LNO observations taken covering more than one full Martian Year reveal the  
562 same general climatological trends that have been observed by other spacecraft (e.g.,  
563 Smith et al., 2009; 2018; Bouche et al., 2021), but with some differences. The global,  
564 annual average value of CO vmr is found to be  $\sim 800$  ppmv for the daylight portions of  
565 Mars observable by the NOMAD LNO observations. A minimum in CO vmr is observed  
566 at high latitudes around the summer solstice in both hemispheres, although the decrease  
567 in CO vmr is much more pronounced in the south than in the north because of the greater  
568 amount of CO<sub>2</sub> released from the seasonal cap in the south. At low latitudes, the seasonal  
569 trend generally follows that expected of a non-condensable gas (e.g., Forget et al., 2008;  
570 Daerden et al., 2019; Holmes et al., 2019) with maximum CO vmr in the season around  
571  $L_s=180^\circ$  as air enriched with CO is transported northward across the equator. Maps of  
572 CO vmr show relatively little spatial variation outside of a noticeable enhancement over  
573 Hellas and other areas of low-lying topography during southern summer. There is no  
574 obvious trend in CO vmr as a function of local time for the daytime hours observed by  
575 NOMAD LNO. Compared to retrievals of CO vmr from CRISM (Smith et al., 2018), the  
576 NOMAD results show less overall variation with the high-latitude summer minima in  
577 each hemisphere having an amplitude roughly half as large.

578 Model results of CO vmr from the GEM-Mars GCM model broadly agree with the  
579 NOMAD LNO retrievals. The correspondence is closer than that between the GEM-Mars  
580 results and the CRISM retrievals of CO vmr (Smith et al., 2018), capturing both the  
581 amplitude of the high-latitude summertime minima and low-latitude seasonal variations  
582 observed by NOMAD. Small differences between the model and retrievals may be  
583 reduced with further improvement in model parameterizations.

584 The ExoMars Trace Gas Orbiter and NOMAD instrument continue to operate at the time  
585 of this writing taking new LNO observations in orders 189 and 190 to characterize CO.  
586 Further observations will extend the existing record of carbon monoxide retrievals to  
587 provide an even better estimate of CO climatology through better statistics and by filling  
588 in the gaps between lobes seen in Fig. 10, and will enable the study of the limits of  
589 interannual variation in CO and the response of CO to large dust storms.

## 590 **Acknowledgements**

591 This work was supported by NASA's Mars Program Office under WBS 604796,  
592 "Participation in the TGO/NOMAD Investigation of Trace Gases on Mars." The  
593 NOMAD experiment is led by the Royal Belgian Institute for Space Aeronomy (IASB-  
594 BIRA), assisted by Co-PI teams from Spain (IAA-CSIC), Italy (INAF-IAPS), and the  
595 United Kingdom (Open University). This project acknowledges funding by the Belgian  
596 Science Policy Office (BELSPO), with the financial and contractual coordination by the  
597 ESA Prodex Office (PEA 4000103401, 4000121493), by Spanish Ministry of Science  
598 and Innovation (MCIU) and by European funds under grants PGC2018-101836-B-I00

599 and ESP2017-87143-R (MINECO/FEDER), as well as by UK Space Agency through  
600 grants ST/V002295/1, ST/P001262/1, ST/R001405/1 and ST/R00145X/1 and Italian  
601 Space Agency through grant 2018-2-HH.0. This work was supported by the Belgian  
602 Fonds de la Recherche Scientifique – FNRS under grant number 30442502 (ET\_HOME).  
603 The IAA/CSIC team acknowledges financial support from the State Agency for Research  
604 of the Spanish MCIU through the ‘Center of Excellence Severo Ochoa’ award for the  
605 Instituto de Astrofísica de Andalucía (SEV-2017-0709). US investigators were supported  
606 by the National Aeronautics and Space Administration. Canadian investigators were  
607 supported by the Canadian Space Agency.”

## References

- Aoki, S., Vandaele, A.C., Daerden, F., et al., 2019. Water vapor vertical profiles on Mars in dust storms observed by TGO/NOMAD. *J. Geophys. Res. Planets*, 124, 3482–3497.
- Billebaud, F., Brillet, J., Lellouch, E., et al., 2009. Observations of CO in the atmosphere of Mars with PFS onboard Mars Express, *Planet. Space Sci.*, 57, 1446–1457.
- Bouche, J., Coheur, P.-F., Giuranna, M., Wolkenberg, P., Nardi, L., Amoroso, M., Vandaele, A.C., Daerden, F., Neary, L., Bauduin, S., 2020. Seasonal and spatial variability of carbon monoxide (CO) in the Martian atmosphere from PFS/MEX observations. *J. Geophys. Res.*, in press.
- Christensen, P.R., Bandfield, J.L., Hamilton, V.E., et al., 2001. The Mars Global Surveyor Thermal Emission Spectrometer experiment: Investigation description and surface science results. *J. Geophys. Res.*, 106, 23,823–23,871.
- Clancy, R.T., Muhleman, D.O., Jakosky, B.M., 1983. Variability of carbon monoxide in the Mars atmosphere. *Icarus*, 55, 282–301.
- Clancy, R.T., Muhleman, D.O., and Berge, G.L., 1990. Global changes in the 0–70 km thermal structure of the Mars atmosphere derived from 1975 to 1989 microwave CO spectra, *J. Geophys. Res.*, 95, 14543–14554.
- Clancy, R.T., M. J. Wolff, M.J., Christensen, P.R., 2003. Mars aerosol studies with the MGS-TES emission phase function observations: Optical depths, particle sizes, and ice cloud types versus latitude and solar longitude, *J. Geophys. Res.*, 108(E9), 5098, doi:10.1029/2003JE002058.
- Daerden, F., Whiteway, J.A., Neary, L., et al., 2015. A solar escalator on Mars: Self-lifting of dust layers by radiative heating. *Geophys. Res. Lett.*, 42, 73197326. doi:10.1002/2015GL064892
- Daerden, F., Neary, L., Viscardy, S., García Muñoz, A., Clancy, R.T., Smith, M.D., Encrenaz, T., Fedorova, A., 2019. Mars atmospheric chemistry simulations with the GEM-Mars general circulation model. *Icarus*, 326, 197–224.
- Encrenaz, T., Fouchet, T., Melchiorri, R., et al., 2006. Seasonal variations of the Martian CO over Hellas as observed by OMEGA/Mars Express, *Astron. Astrophys.*, 459, 265–270.
- Forget, F., Hourdin, F., Fournier, R., Hourdin, C., Talagrand, O., 1999. Improved general circulation models of the Martian atmosphere from the surface to above 80 km. *J. Geophys. Res.*, 104, E10, 24,155–24,175.
- Forget, F., Millour E., Montabone, L., Lefèvre, F., 2008. Non condensable gas enrichment and depletion in the Martian polar regions, paper presented at Third International Workshop on the Mars Atmosphere: Modeling and Observations, Lunar and Planet. Inst., Williamsburg, Va., 10–13 Nov.
- Goody, R.M., Yung, Y.L., 1989. *Atmospheric Radiation: Theoretical Basis*, Oxford Univ. Press, New York.
- Gordon, L.E., Rothman, L.S., Hill, C., et al., 2017. The HITRAN2016 molecular spectroscopic database. *J. Quant. Spectrosc. Rad. Transf.*, 203, 3–69.
- Guzewich, S.D., Lemmon, M., Smith, C.L., et al., 2018. Mars Science Laboratory observations of the 2018/Mars Year 34 global dust storm. *Geophys. Res. Lett.*, 46, doi:10.1029/2018GL080839.

- Holmes, J.A., Lewis, S.R., Patel, M.R., Smith, M.D., 2019. Global analysis and forecasts of carbon monoxide on Mars. *Icarus*, 326, 232–245.
- Holmes, J.A., Lewis, S.R., Patel, M.R., 2020. OpenMARS: A global record of martian weather from 1999 to 2015. *Planet. Space Sci.*, 188, 104969. doi:10.1016/j.pss.2020.104962.
- Kaplan, L.D., Connes, J., Connes, P., 1969. Carbon monoxide in the Martian atmosphere. *Astrophys. J.*, 157, L187–L192.
- Korablev, O., Vandaele, A.C., Montmessin, F., et al., 2019. No detection of methane on Mars from early ExoMars Trace Gas Orbiter observations. *Nature*, 568, 517–520, doi:10.1038/s41586-019-1096-4.
- Krasnopolsky, V.A., 2003. Spectroscopic mapping of Mars CO mixing ratio: Detection of north-south asymmetry, *J. Geophys. Res.*, 108, 5010, doi:10.1029/2002JE001926.
- Krasnopolsky, V.A., 2007. Long-term spectroscopic observations of Mars using IRTF/CSHELL: Mapping of O<sub>2</sub> dayglow, CO, and search for CH<sub>4</sub>, *Icarus*, 190, 93–102.
- Lacis, A.A., Oinas, V., 1991. A description of the correlated-k distribution method for modeling nongray gaseous absorption, thermal emission, and multiple scattering in vertically inhomogeneous atmospheres, *J. Geophys. Res.*, 96, 9027 – 9063.
- Lefèvre, F., Krasnopolsky, V., 2017. Atmospheric Photochemistry, Chapter 13 in “The Atmosphere and Climate of Mars”, Cambridge University Press. doi:10.1017/9781139060172.013.
- Lellouch, E., Paubert, G., and Encrenaz, T., 1991. Mapping of CO millimeter-wave lines in Mars atmosphere: the spatial distribution of carbon monoxide on Mars, *Planet. Space Sci.*, 39, 219–224.
- Lian, Y., Richardson, M.I., Newman, C.E., Lee, C., Toigo, A.D., Mischna, M.A., Campin, J.-M., 2012. The Ashima/MIT Mars GCM and argon in the martian atmosphere, *Icarus*, 218, 1043–1070. doi:10.1016/j.icarus.2012.02.012
- Liuzzi, G., Villanueva, G.L., Mumma, M.J., Smith, M.D., Daerden, F., Ristic, B., Thomas, I., Vandaele, A.C., Patel, M.R., Lopez-Moreno, J.-J., Bellucci, G., and the NOMAD team, 2019. Methane on Mars: New insights into the sensitivity of CH<sub>4</sub> with the NOMAD/ExoMars spectrometer through its first in-flight calibration, *Icarus*, 321, 671–690.
- Martínez, G.M., Newman, C.N., Vicente-Retortillo, Á., et al., 2017. The modern near-surface Martian climate: A review of in-situ meteorological data from Viking to Curiosity. *Space Sci. Rev.*, doi:10.1007/s11214-017-0360-x.
- Millour, E., Forget, F., Spiga, A., Vals, M., Zakharov, V., Montabone, L., Lefèvre, F., Montmessin, F., Chaufray, J.-Y., López-Valverde, M.A., González-Galindo, F., Lewis, S.R., Read, P.L., Desjean, M.-C., Cipriani, F., and the MCD development team. The Mars Climate Database (version 5.3). Presented at the “From Mars Express to ExoMars” Scientific Workshop, 27–28 February 2018, Madrid, Spain.
- Montabone, L., Forget, F., Millour, E., Wilson, R.J., Lewis, S.R., Cantor, B. Kass, D., Kleinböhl, A., Lemmon, M.T., Smith, M.D., Wolff, M.J., 2015. Eight-year climatology of dust optical depth on Mars. *Icarus*, 251, 65–95.
- Montabone, L., Spiga, A., Kass, D.M., Kleinböhl, A., Forget, F., Millour, E., 2020. Martian Year 34 column dust climatology from Mars Climate Sounder

- Observations: Reconstructed maps and model simulations. *J. Geophys. Res.*, 125, e2019JE006111.
- Moreno, R., Lellouch, E., Forget, F., Encrenaz, T., Guilloteau, S., Millour, E., 2009. Wind measurements in the Mars' middle atmosphere: IRAM Plateau de Bure interferometric CO observations. *Icarus* 201, 549–563.
- Neary, L., Daerden, F., 2018. The GEM-Mars General Circulation Model for Mars: Description and Evaluation, *Icarus*, 300, 458–476, doi:10.1016/j.icarus.2017.09.028.
- Neary, L., Daerden, F., Aoki, S., Whiteway, J., Clancy, R. T., Smith, M., et al., 2020. Explanation for the increase in high-altitude water on Mars observed by NOMAD during the 2018 global dust storm. *Geophys. Res. Lett.*, 47, e2019GL084354, doi:10.109/2019GL084354.
- Nevejans, D., Neefs, E., Van Ransbeeck, E., Berkenbosch, S., Clairquin, R., De Vos, L., Moelans, W., Glorieux, S., Baeke, A., Korablev, O., Vinogradov, I., Kalinnikov, Y., Bach, B., Dubois, J.P., Villard, E., 2006. Compact high-resolution spaceborne echelle grating spectrometer with AOTF based on order sorting for the infrared domain from 2.2 to 4.3 micrometer. *Appl. Opt.*, 45, 5191–5206.
- Patel, M.R., Antoine, P., Mason, J.P., Leese, M.R., Hathi, B., Stevens, A.H., Dawson, D., Gow, J.P.D., Ringrose, T.J., et al., 2017. NOMAD spectrometer on the ExoMars trace gas orbiter mission: Part 2 – design, manufacturing, and testing of the ultraviolet and visible channel. *Appl. Opt.*, 56, 2771–2782.
- Sindoni, G., Formisano, V., Geminale, A., 2011. Observations of water vapour and carbon monoxide in the Martian atmosphere with the SWC of PFS/MEX. *Planet. Space Sci.*, 59, 149–162.
- Smith, M.D., Wolff, M.J., Clancy, R.T., Murchie, S.L., 2009. Compact Reconnaissance Imaging Spectrometer observations of water vapor and carbon monoxide, *J. Geophys. Res.*, 114, E00D03, doi:10.1029/2008JE003288.
- Smith, M.D., Daerden, F., Neary, L., Khayat, A., 2018. The climatology of carbon monoxide and water vapor on Mars as observed by CRISM and modeled by the GEM-Mars general circulation model. *Icarus*, 301, 117–131.
- Smith, M.D., 2018. Local time variation of water ice clouds on Mars as observed by THEMIS. *Icarus*, 333, 273–282.
- Smith, M.D., 2019. THEMIS observations of the 2018 Mars global dust storm. *J. Geophys. Res. Planets*, 124, doi:10.1029/2019JE006107.
- Thomas, G.E., Stamnes, K., 1999. *Radiative transfer in the atmosphere and ocean*. Cambridge Univ. Press, Cambridge.
- Thomas, I., et al., 2020. Radiometric calibration of NOMAD observations. In preparation.
- Tillman, J.E., Johnson, N.C., Guttorp, P., Percival, D.B., 1993. The Martian annual atmospheric pressure cycle: Years without great dust storms, *J. Geophys. Res.*, 98, E6, 10963–10971.
- Titov, D.V., Svedhem, H., McCoy, D., et al., 2006. Venus express: Scientific goals, instrumentation and scenario of the mission. *Cosm. Res.*, 44, 334–348.
- Vandaele, A.C., Neefs, E., Drummond, R., et al., 2015. Science objectives and performances of NOMAD, a spectrometer suite for the ExoMars TGO mission, *Planet. Space Sci.*, 119, 233–249.

- Vandaele, A.C., Lopez-Moreno, J.-J., Patel, M.R., et al., 2018. NOMAD, an integrated suite of three spectrometers for the ExoMars Trace Gas Mission: Technical description, science objectives and expected performance. *Space Sci. Rev.* 214:80, doi:10.1007/s11214-018-0517-2.
- Vandaele, A.C., Korabiev, O., Daerden, F., et al., 2019. Martian dust storm impact on atmospheric H<sub>2</sub>O and D/H observed by ExoMars Trace Gas Orbiter. *Nature*, 568, 521–525, doi:10.1038/s41586-019-1097-3.
- Vincente-Retortillo, Á, Martínez, G.M., Renno, N.O., Lemmon, M.T., de la Torre-Juárez, M., 2017. Determination of dust aerosol particle size at Gale Crater using REMS UVS and Mastcam measurements. *Geophys. Res. Lett.*, 44, doi:10.1002/2017GL072589.
- Viscardy, S., Daerden, F., Neary L., 2016. Formation of layers of methane in the atmosphere of Mars after surface release, *Geophys. Res. Lett.*, 43, 5, 1868–1875, doi:10.1002/2015GL067443.
- Wolff, M.J., Clancy, R.T., 2003. Constraints on the size of martian aerosols from Thermal Emission Spectrometer observations. *J. Geophys. Res.* 108, 5097. <http://dx.doi.org/10.1029/2003JE002057>.
- Wolff, M.J., et al., 2006. Constraints on dust aerosols from the Mars Exploration Rovers using MGS overflights and Mini-TES. *J. Geophys. Res.* 111, E12S17, <http://dx.doi.org/10.1029/2006JE002786>.
- Wolff, M.J., et al., 2009. Wavelength dependence of dust aerosol single scattering albedo as observed by the Compact Reconnaissance Imaging Spectrometer. *J. Geophys. Res.* 114, E00D04, <http://dx.doi.org/10.1029/2009JE00350>.

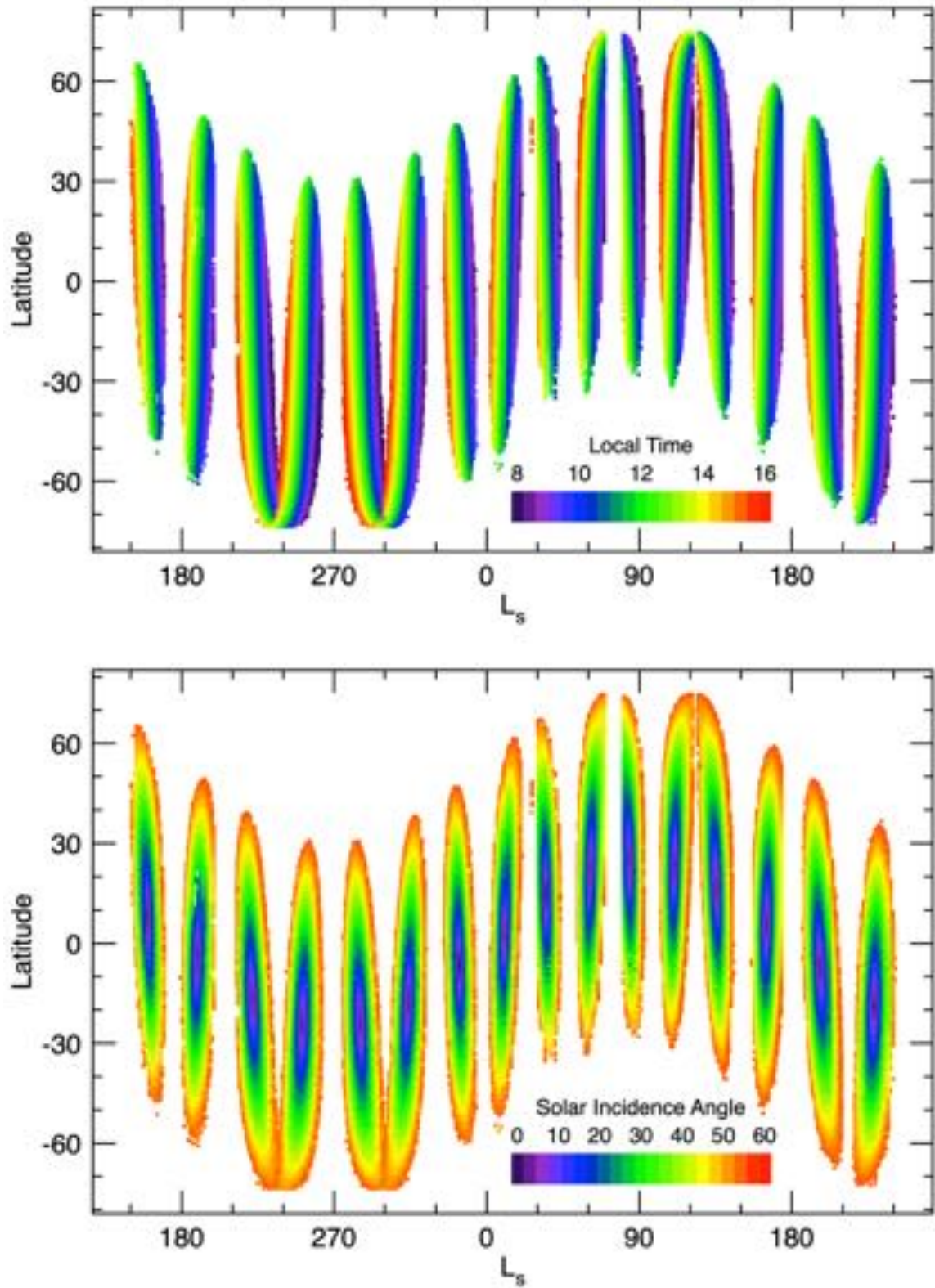


**Figure 1.** The seasonal and latitudinal coverage of the NOMAD LNO observations in orders 189 and 190 used in this study. Shown are (top) the local true solar time for each observation, and (bottom) the solar incidence angle.

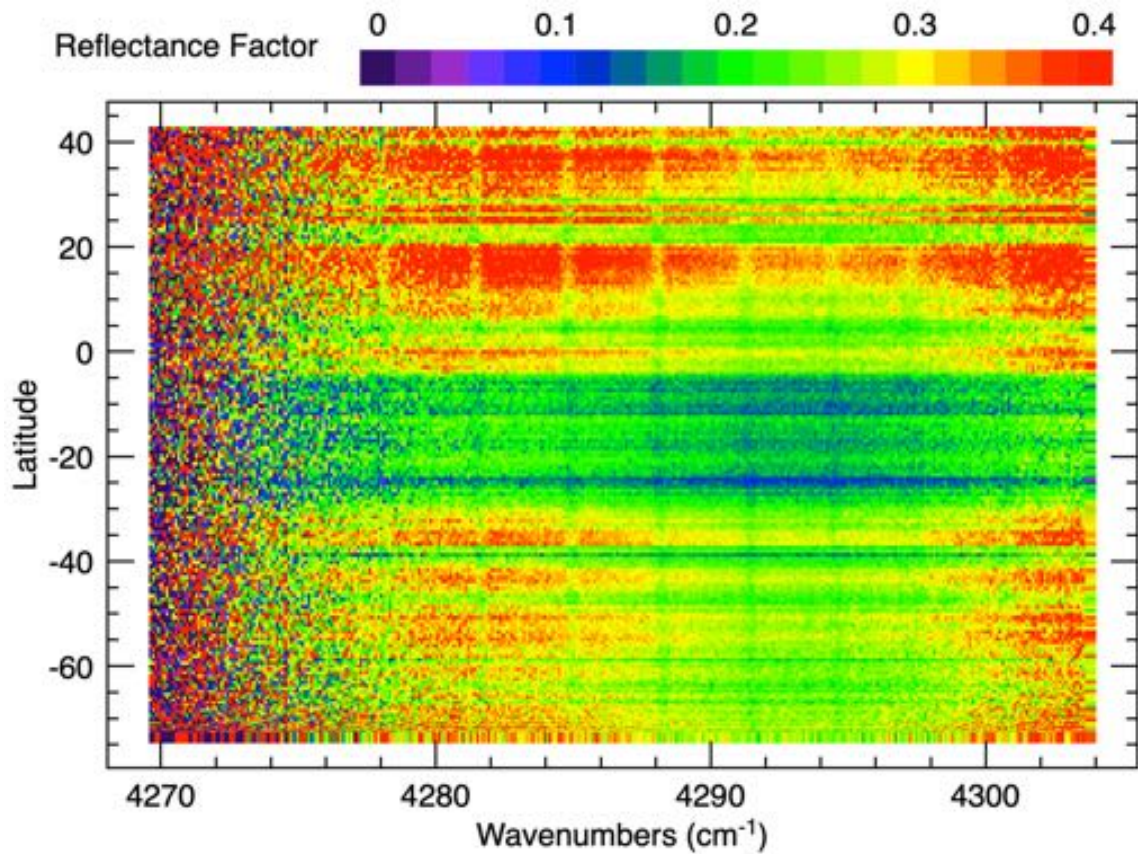


**Figure 2.** A typical NOMAD LNO observation for order 190 shown in terms of reflectance factor. The data were taken on 5 November 2018 (MY 34,  $L_s=283^\circ$ ). Spectral features caused by CO are visible as vertical lines in the image. In this representation, the continuum level signal is controlled largely by surface albedo, solar incidence angle, and aerosol scattering.



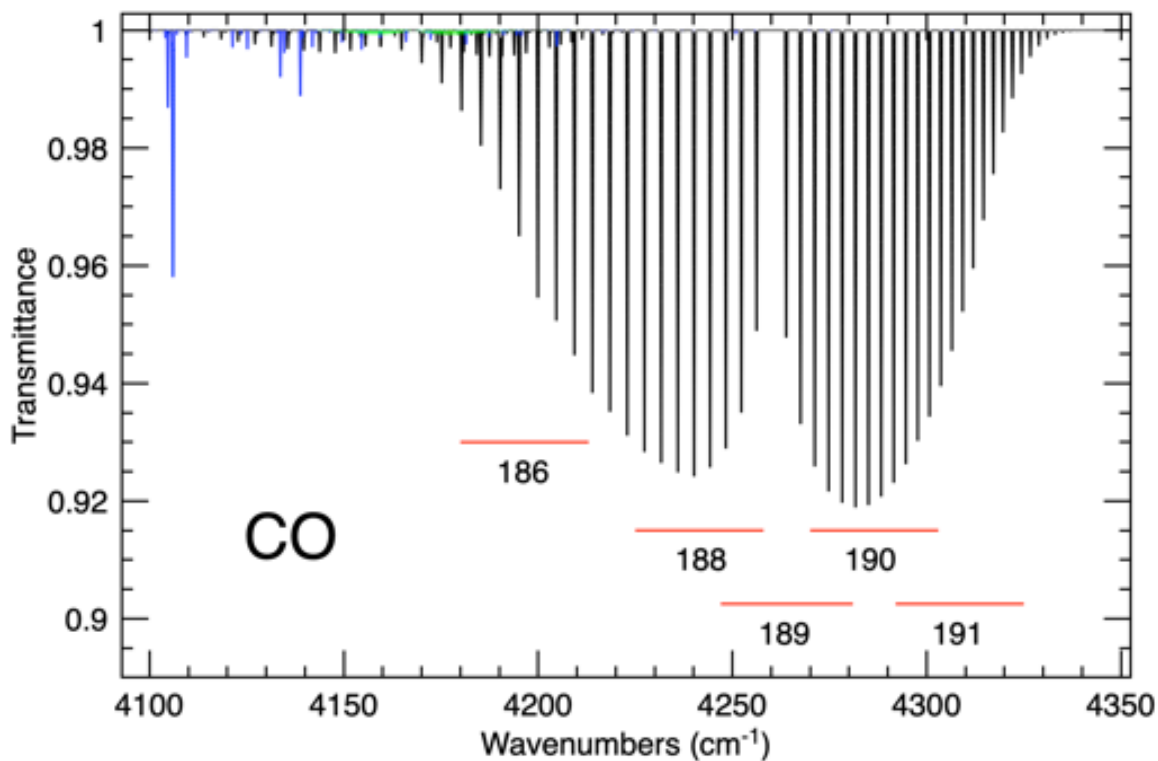


**Figure 3.** A computed spectrum of the absorptions from CO (black), water vapor (blue), and CO<sub>2</sub> (green) convolved to a spectral resolution of 0.4 cm<sup>-1</sup>. The spectral range covered by different NOMAD LNO grating orders are indicated by the numbers 186 through 191. The orders used in this study (189 and 190) contain strong CO lines with no interference from other gases.

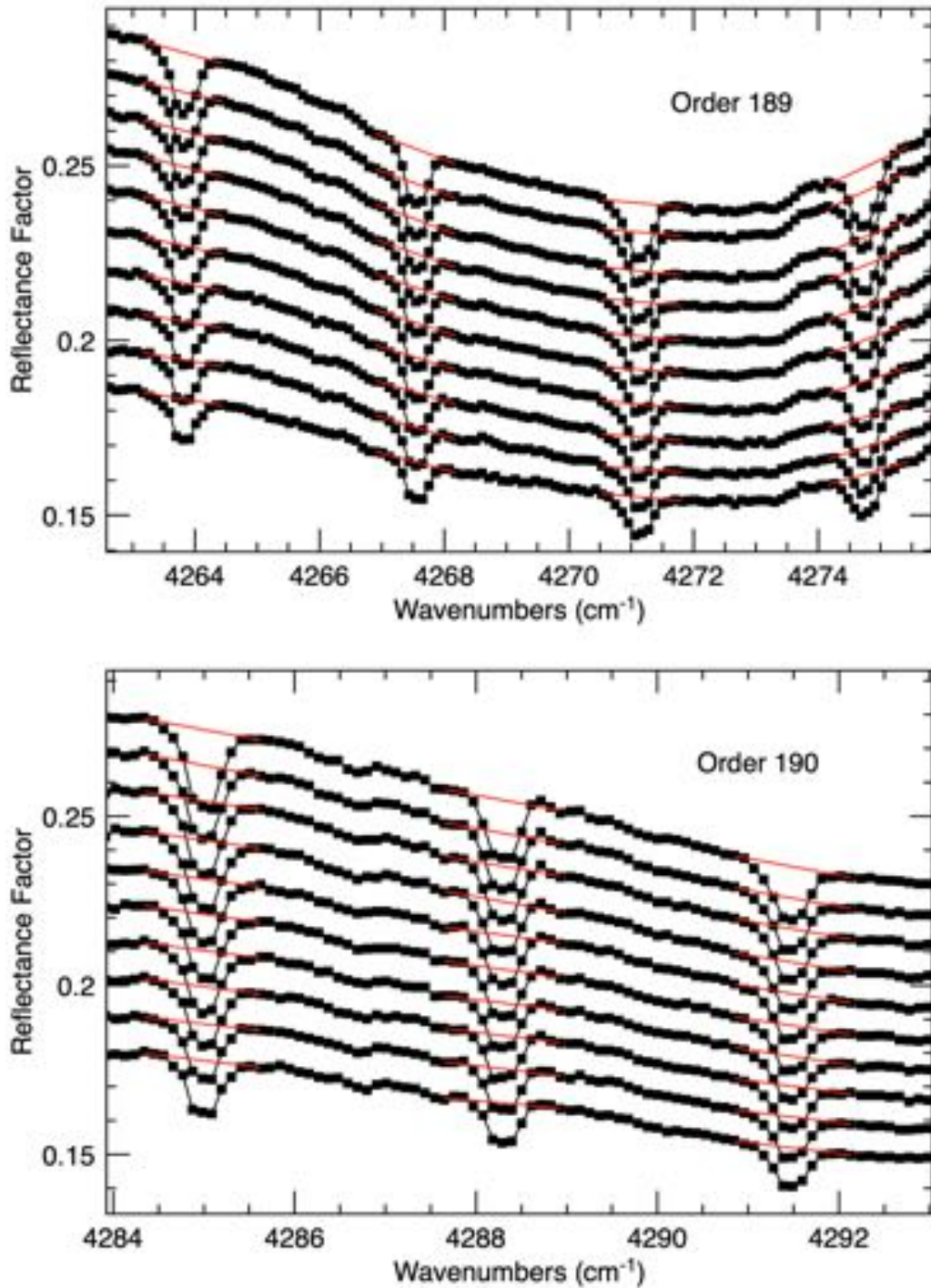


**Figure 4.** Averaged spectra for (top) order 189 and (bottom) order 190 showing the CO absorptions used for the retrieval. These are lines from the (2-0) ro-vibrational band of CO, lines R0, R1, R2, and R3 for order 189, and R6, R7, and R8 for order 190. The red line segments show the estimated continua and the spectral range over which the integrated line depths are computed for each line.

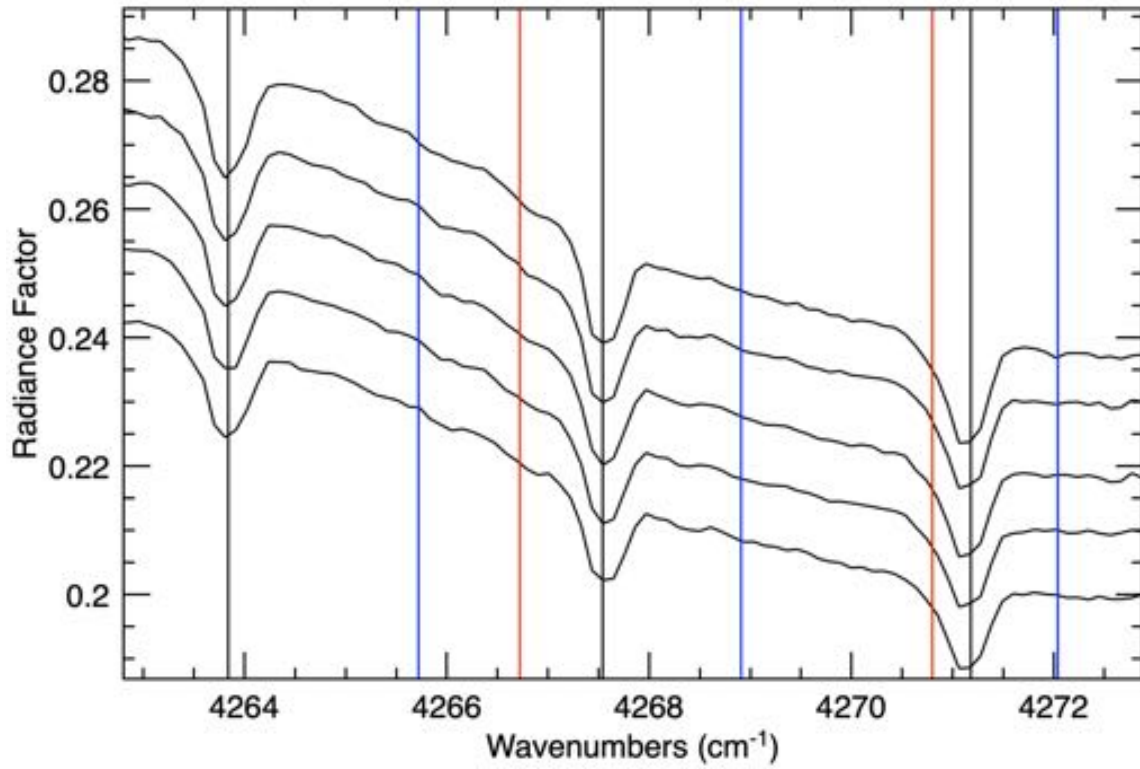


**Figure 5.** Averaged spectra for order 189 showing the expected spectral locations of spectral features. The black vertical lines show the frequencies of three of the main CO lines in order 189. The red and blue vertical lines show the frequencies where CO absorptions from orders 188 (red) and 190 (blue) would appear if aliased by the AOTF.

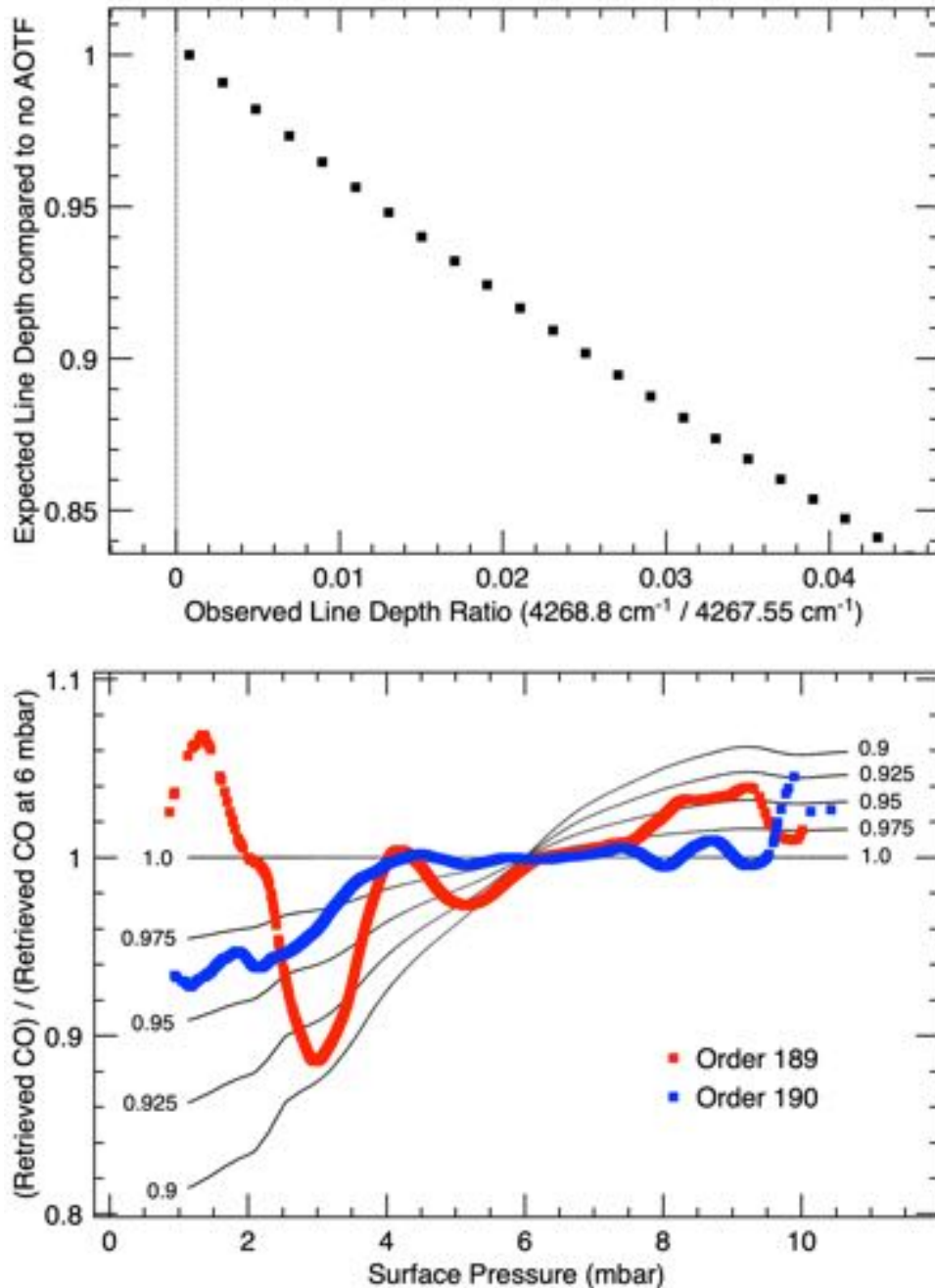


**Figure 6.** Two ways to estimate the continuum contribution from neighboring orders from the AOTF. (Top panel) The expected line depth of CO lines as a fraction of that with no AOTF is shown as a function of the observed line depth of a CO absorption aliased from a neighboring order (4268.8 cm<sup>-1</sup>, the middle blue line in Fig. 5) against the observed line depth of a CO absorption from the order being observed (4267.55 cm<sup>-1</sup>, the middle black line in Fig. 5). (Bottom panel) For line depths multiplied by a given constant value (the numbers given at each end of the black lines), the retrieved CO vmr as a function of surface pressure has a systematic variation as shown by the black curves. The CO vmr retrieved from the observations (red and blue points) are consistent with this factor being 0.95 or greater.

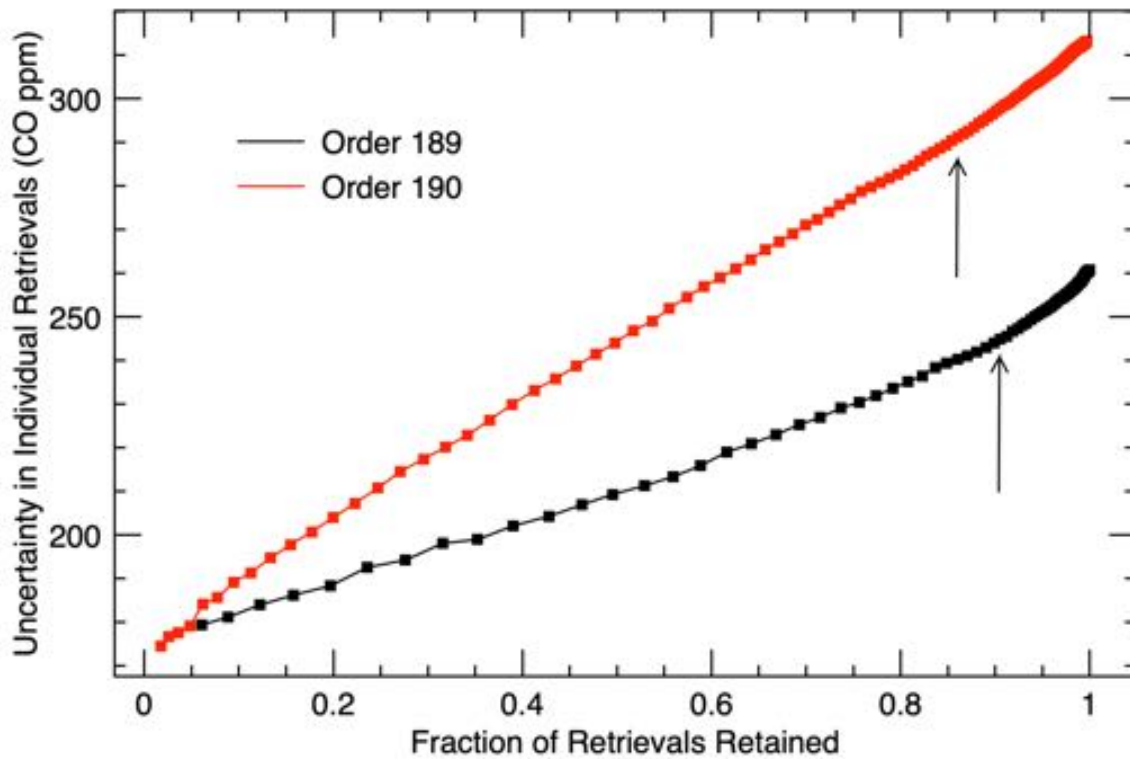


**Figure 7.** The observed level of uncertainty in the retrieved value of CO vmr as a function of the fraction of retrievals retained. Each point represents a different upper limit for the maximum allowed noise level in the observations. The arrows show the selected upper limit for each order.

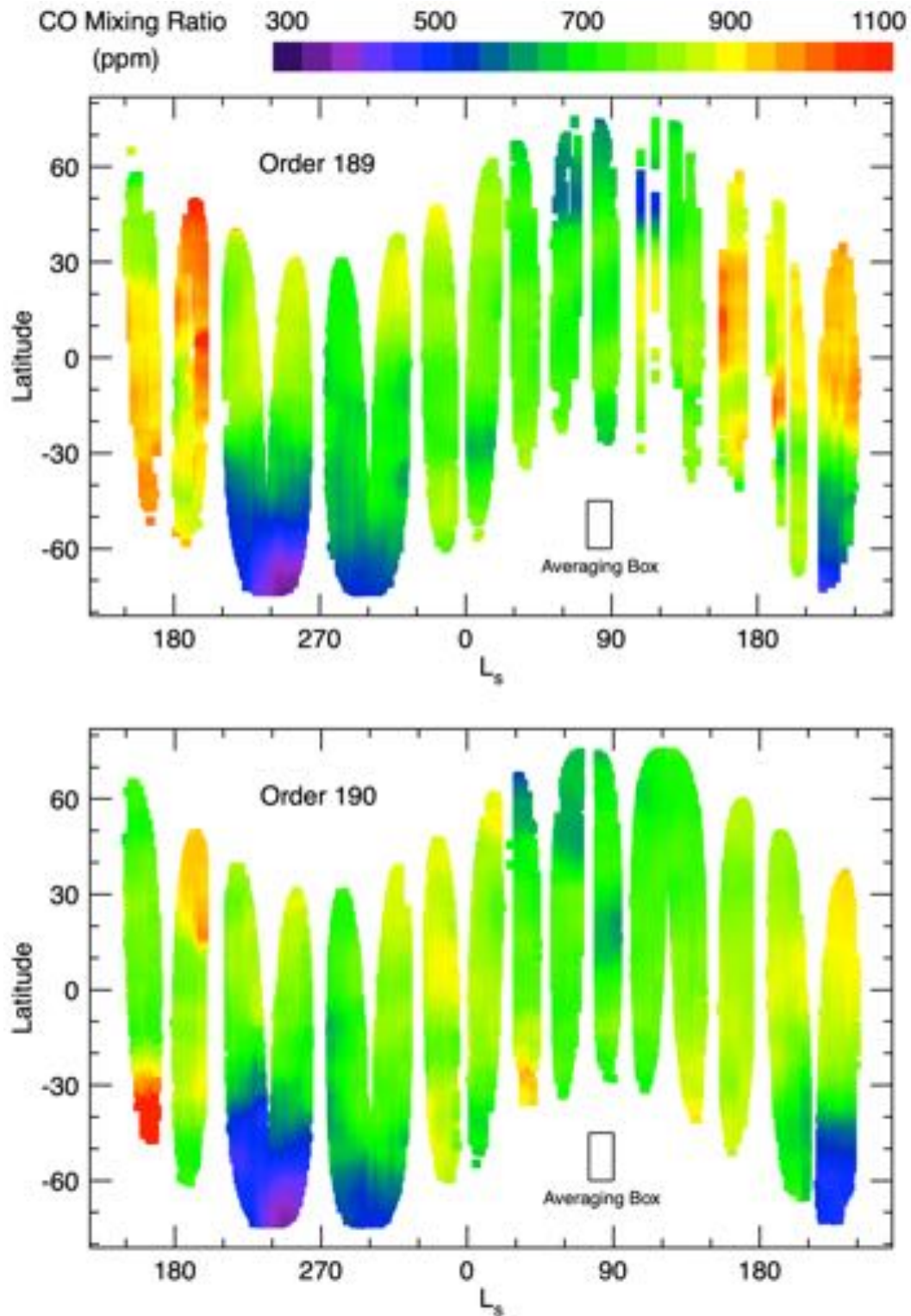


**Figure 8.** The column-averaged carbon monoxide volume mixing ratio retrieved from NOMAD LNO spectra as a function of season, latitude, and grating order.

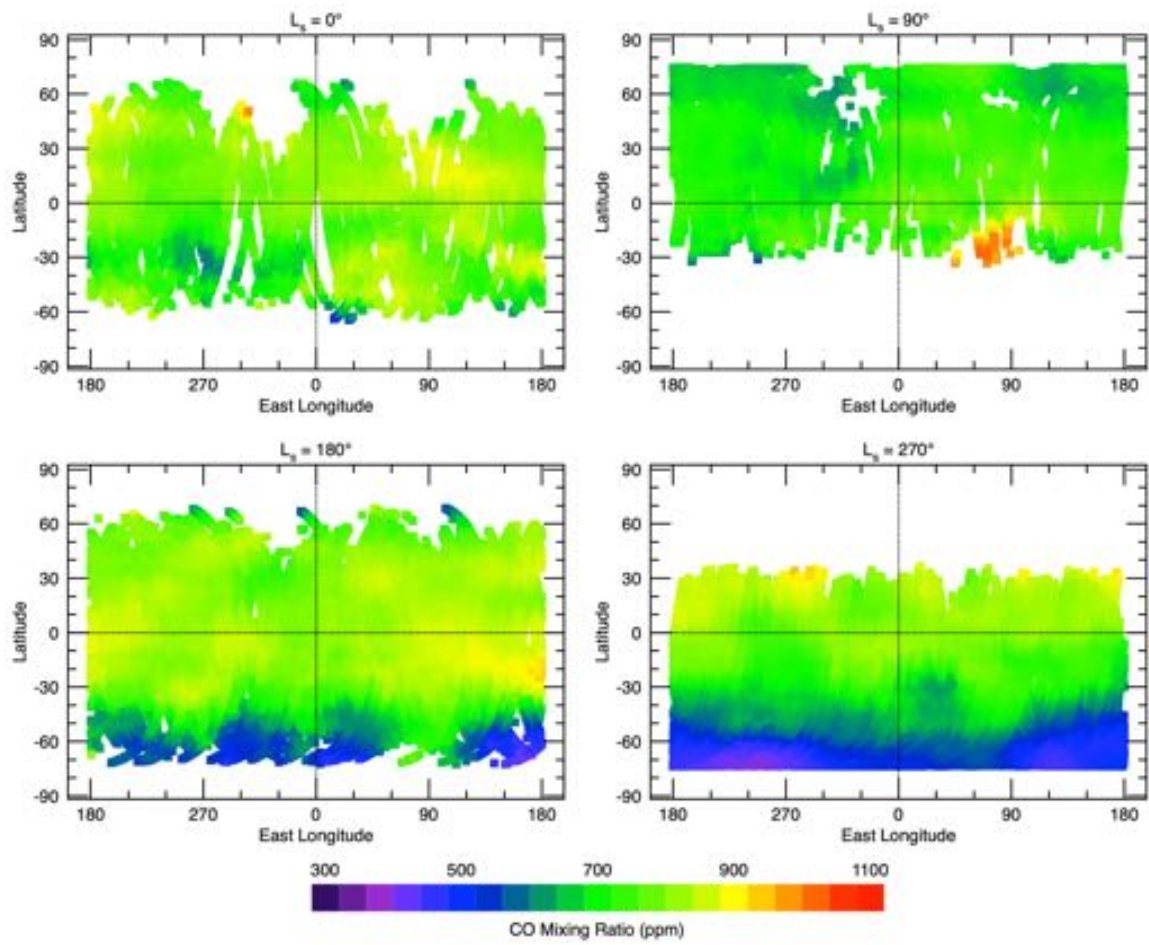


**Figure 9.** Maps showing the spatial variation of CO vmr retrieved from NOMAD LNO spectra for four different seasons.

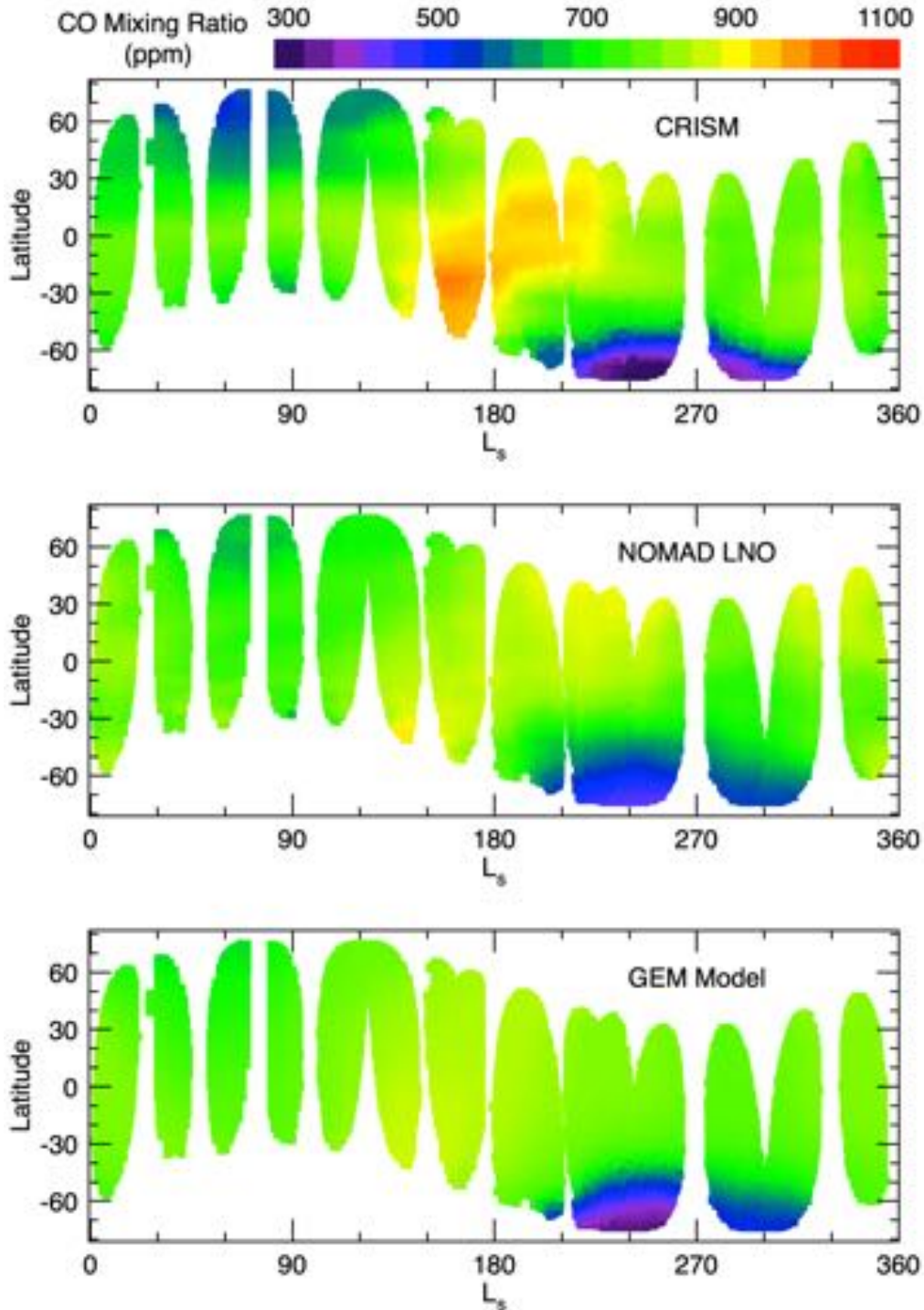


**Figure 10.** A comparison of CO vmr climatologies from (top) CRISM, (middle) NOMAD LNO, and (bottom) the GEM-Mars model. The CRISM and GEM-Mars model data have been interpolated to the times and locations of the NOMAD LNO retrievals, and all three datasets have been smoothed ( $45^\circ$  in  $L_s$  and  $15^\circ$  in latitude) for easier comparison.



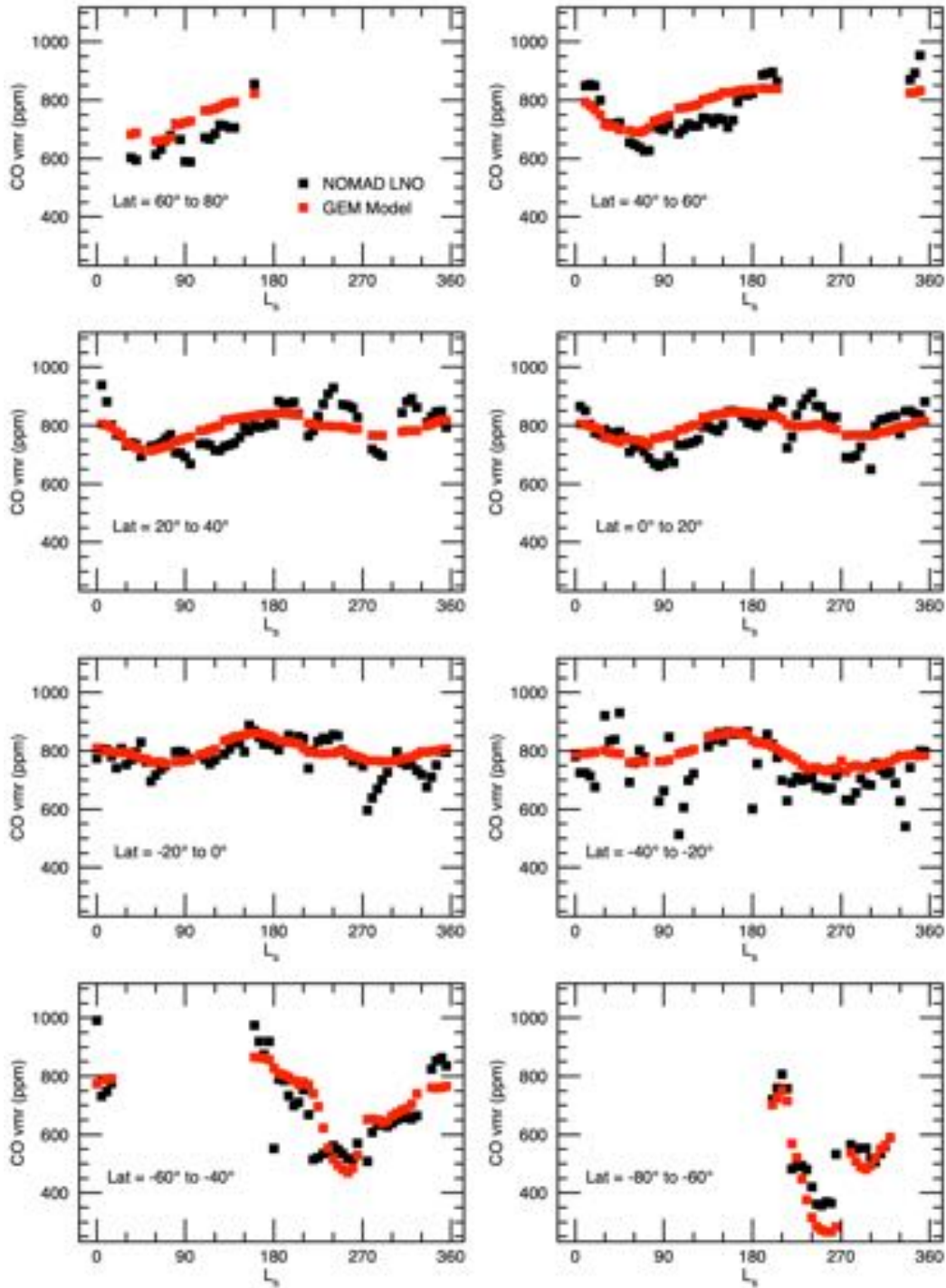


**Figure 11.** Comparison of GEM-Mars model simulation of CO vmr (red points) with NOMAD LNO retrievals of CO vmr (black points). Both datasets have been binned  $15^\circ$  in  $L_s$ .